ADVANCES IN GEOMATICS

VOLUME 01 • ISSUE 01 • OCTOBER 2023
e-ISSN: 3023-4980

ORIGINAL ARTICLE

Submission: 04/08/2023
Accepted: 03/10/2023

PRE-EARTHQUAKE IONOSPHERIC PERTURBATION ANALYSIS USING DEEP LEARNING TECHNIQUES

Mohd SAQIB[1] **Muhammad Arqim ADIL**[2] **Mohamed FREESHAH**[3-4*]

[1] Department of Mathematics and Computing, Indian Institute of Technology (ISM), Dhanbad, Jharkhand, India.

[2] Department of GNSS, Institute of Space Technology, Islamabad, Pakistan.

[3] School of Geodesy and Geomatics, Wuhan University, Wuhan, China.

[4] Geomatics Engineering Department, Faculty of Engineering at Shoubra, Benha University, Cairo, Egypt.

* Corresponding Author: M. Freeshah, engmfreeshah@yahoo.com

ABSTRACT

It has been observed in many studies that ionosphere create a significant perturbation before major earthquakes. Therefore, forecasting of earthquakes on the basis of the ionosperic anomalies become trending. However, we still need more accurate and reliable advance technique to predict. In this study, we have analysed the Awaran, Pakistan (Mw 7.7) earthquake and associated Total Electron Content (TEC) anomalies which was happended on 24 Sep, 2013 using long short-term memory (LSTM) network model. We have recorded data from Global Navigation Satellite System (GNSS) for the proposed study with a 2-h temporal of 45 days. Afterwards, we set the hyperparameters, train the model on the dataset and maintain a prediction with high accuracy (0.07 TECU Loss). We performed the forecasting model on two different regions to differentiate the observed anomalies as pure seismic precursors without any external influence in the ionosphere. In this regard, we constructed one TEC time series right above the Awaran earthquake epicenter and one for a point located outside the earthquake preparation area (EPA). The results demonstrated that strong positive anomalies found on Sep 21, 3 days before the Awaran earthquake within EPA, which is consistent with findings of the previous studies. The occurrence of these irregularities can be attributed to the Awaran earthquake, which can be attributed to the calm space weather conditions during those days. On the other hand, none of the similar anomalies exist outside the EPA. Our study presents new insight into the AI techniques in seismo-ionospheric earthquake forecasting.

Keywords: Anomaly Detection, Earthquake Forecast, Long Short Term Memory, Time Series Analysis, Total Electron Content.

Cited As:

Saqib, M., Adil, M. A., & Freeshah, M. (2023). Pre-earthquake Ionospheric Perturbation Analysis using Deep Learning Techniques, Advances in Geomatics, 1(1), 48-67. https://doi.org/10.5281/zenodo.10202326

INTRODUCTION

Earthquakes are considered the most devastating natural disasters, leading to the loss of countless human lives and significant economic damage (Athukorala and Resosudarmo, 2005). Scientists believe that earthquake forecasting may be a difficult task but not an impossible one. Some modern-day researchers are having appreciable endeavors in the search of any potential seismic signal prior to the major earthquakes that could serve as a possible seismic precursor. Many studies have widely reported the ionospheric electron density variations as potential seismic precursors some few days before earthquakes (Hattori et al., 2014, Adil et al., 2021a). Nevertheless, these approaches primarily rely on statistical analysis or intricate mathematical models. Hence, the utilization of Artificial Intelligence (AI) has the potential to introduce groundbreaking advancements in earthquake prediction by leveraging ionospheric anomalies.

Numerous scholars have extensively investigated various theories and evidence in order to understand the underlying cause of the correlation between seismic activity and the ionosphere. For instance, Klimenko et al. (2011) have proposed a mechanism that explains how ionospheric perturbations occur because of electric fields generated by intense internal gravity waves. Rozhnoi et al. (2007) have examined the strong coupling between the lithosphere and ionosphere through gravity waves, providing case studies of three significant earthquakes (M>7) that occurred in Japan in November 2004. Pulinets and Ouzounov (2011) proposed a more detailed lithosphere-atmosphere-ionosphere coupling hypothesis based on the release of a radon gas during the deformation process of seismic activity. They proposed that the radon gas reacts with the atmospheric gases that alter the air temperature and humidity as well as forming an anomalous thermal cloud at the top of the atmosphere as OLR. These atmospheric circulations induce vertical electric field that variates the electron concentrations in the ionosphere. Adil et al. (2021b) investigated two back to back earthquakes in the Taiwan region and validated the hypothesis of the Pulinets and Ouzounov (2011) using satellite measurements.

However, further statistical analysis is required to determine the underlying physical mechanisms behind this correlation. Numerous studies have conducted statistical analyses of Total Electron Content (TEC) values prior to significant earthquakes, providing insights into the potential for earthquake forecasting using ionospheric precursors (Akhoondzadeh et al., 2010; Liu et al., 2013; Guo et al., 2015; Shi et al., 2017; Li et al., 2018a). The ionospheric disturbances preceding the Tohoku earthquake (M=9) on March 11, 2011, in Japan were investigated by Ouzounov et al. (2011) and Liu et al. (2019). In Liu et al. (2019), the authors examined the variations in TEC seven days prior to (and also fifteen days following) the Tohoku earthquake (Mw=9.0) on March 11, 2011, utilizing data from the FORMOSAT-3/COSMIC satellite. This method is accurate but useful for post-analysis of the earthquake as well as another natural disaster e.g., ionospheric anomalies-based precursor also discussed in Hsiao et al. (2010) the study using GNSS for the earthquake of Wenchuan, China (Mw=7.9). On the other hand, the ionospheric perturbation was also detected before another natural disaster e.g.

typhoons, tsunamis, etc. (Li et al., 2018a; Liu et al., 2019; Freeshah et al., 2021).

Emerging fields such as AI, machine learning, sensing techniques, and the Internet of Things (IoT) have found applications in various domains of seismology. For instance, Adeli and Panakkat (2009) utilized these technologies for earthquake magnitude prediction, while Andreadis et al. (2007) employed them for seismic signal acceleration classification. Beyreuther and Wassermann (2008) focused on earthquake detection and seismic arrival prediction. ML techniques have also been used to differentiate earthquake and non-earthquake events based on P-wave and S-wave arrival times, as demonstrated by Li et al. (2018b). Another study introduced a generative adversarial network (GAN) for automatic feature extraction and trained a Random Forest classifier on a dataset of approximately 700,000 earthquake and noise waveforms, achieving high accuracy in recognizing earthquake P waves and noise signals (Li et al., 2018c).

Considering the significance of TEC values for robust earthquake forecasting, Zhukov et al. (2021) developed a model using the XGBoost learning algorithm to estimate TEC values, yielding more accurate results than traditional approaches. Akhoondzadeh (2013) utilized a genetic algorithm to predict TEC values before the Solomon earthquake (M=8) and determined that deviations exceeding predefined upper/lower limits in the predicted and actual TECs could indicate anomalies in the TEC time series. Furthermore, Draz et al. (2023) pioneered in employing deep machine learning to discern ionospheric and atmospheric precursors pertinent to the 2021 Mw 7.1 Japan Earthquake, utilizing parameters like Sea Surface Temperature (SST), Air Temperature (AT), and TEC, and leveraging methodologies such as STDEV and wavelet transformation to pinpoint pre- and post-seismic anomalies. Concurrently, Dilmaghani (2020) delved into the interplay between substantial earthquakes and ionospheric electron density, utilizing GPS data and focusing on the Azerbaijan Earthquakes, underscoring the pivotal role of TEC as a projection of electron density along the signal path from the satellite to the ground receiver. However, it is noteworthy that both studies employed traditional methods, which exhibited limitations when dealing with sequential data like VTEC.

In a parallel vein, Melgarejo-Morales et al. (2023) adeptly applied the Support Vector Machine (SVM) model, utilizing GPS VTEC and space weather parameters to discern ionospheric disturbances potentially correlated with earthquakes, achieving an accuracy of 88.9% and 80% for the training and test sets respectively. Similarly, Asaly et al. (2022) also employed SVM. However, both studies have low score of accuracy.

Hafeez et al. (2022) explores the significance of satellite-based thermal anomalies, particularly Land Surface Temperature (LST) from the MODIS satellite, as substantial precursors for potent earthquakes, exemplified by monitoring variations before and after the Awaran Pakistan earthquake in 2013 (Mw 7.7), the same earthquake explore in the proposed studies. Various detection techniques, including IQR, wavelet transformation, ARIMA, and Neural Network, were employed to identify a

consistent monitoring time window for pre- and post-seismic LST irregularities. Furthermore, Saqib et al. (2022) conducted a comparative analysis of LSTM network models and autoregressive integrated moving average (ARIMA) in detecting ionospheric anomalies, with a particular focus on the Haiti (Mw = 7.0) earthquake, concluding that LSTM exhibited superior performance in detecting seismoionospheric anomalies. The studies collectively underscore the potential and efficacy of machine learning techniques, particularly LSTM networks, in detecting atmospheric and ionospheric precursors to seismic activities, thereby substantiating the application of LSTM in the proposed study as a methodologically sound approach to exploring and predicting earthquake-related anomalies in atmospheric and ionospheric parameters.

1. MODELING AND EVALUATION

In this section, we discuss the data, model generation, evaluation metrics of the model, and its implementation using programing language and platform. We have also analyzed the space weather conditions on the same day.

1.1. Data Description

For our analysis and evaluation of the proposed model, we have chosen a significant earthquake with a magnitude of 7.7 (Mw=7.7). The earthquake under consideration is the Awaran earthquake, which took place on September 24, 2013, at 11:29:47 (UTC). Its epicenter was located 61 km north-northeast (NNE) of Awaran, Pakistan, at coordinates 26.95°N and 65.50°E. Once the earthquake event was finalized, we obtained the corresponding Total Electron Content (TEC) values from the same coordinates and time. TEC is measured in TECU (Total Electron Content Unit), where 1 TECU is equivalent to 1016 electrons per square meter. The ionospheric TEC data used in our study were obtained from the Crustal Dynamics Data Information System (CDDIS).

To detect earthquake-induced ionospheric anomalies, the earthquake preparation area (EPA) of the Awaran earthquake was determined by the formula, r = 100.43*Magnitude, proposed in (Dobrovolsky et al., 1979). EPA of the Awaran earthquake is found to be 2046.4 km. Considering the local behavior of seismo ionospheric anomalies, we analyzed pre-earthquake ionospheric anomalies by obtaining TEC time series at three different locations (epicenter, inside, and outside the EPA). According to this approach, while ionospheric disturbances are expected in and around the epicenter, no significant disturbances are expected outside of the EPA. The geographical and geomagnetic locations of the selected points are demonstrated in Figure 1 and given in Table 1. The geomagnetic coordinates of points were obtained from the WDC for Geomagnetism, Kyoto (http://wdc.kugi.kyoto-u.ac.jp/igrf/gggm/).

Table 1. Geographical and geomagnetic coordinates of selected points.

Location	Geo. Lat. (°N)	Geo. Long. (°E)	Mag. Lat. (°N)	Mag. Long. (°E)
Epicenter	26.95	65.50	19.35	140.68
Within EPA	22.00	70.00	13.99	144.35
Outside EPA	39.00	42.00	34.24	120.90

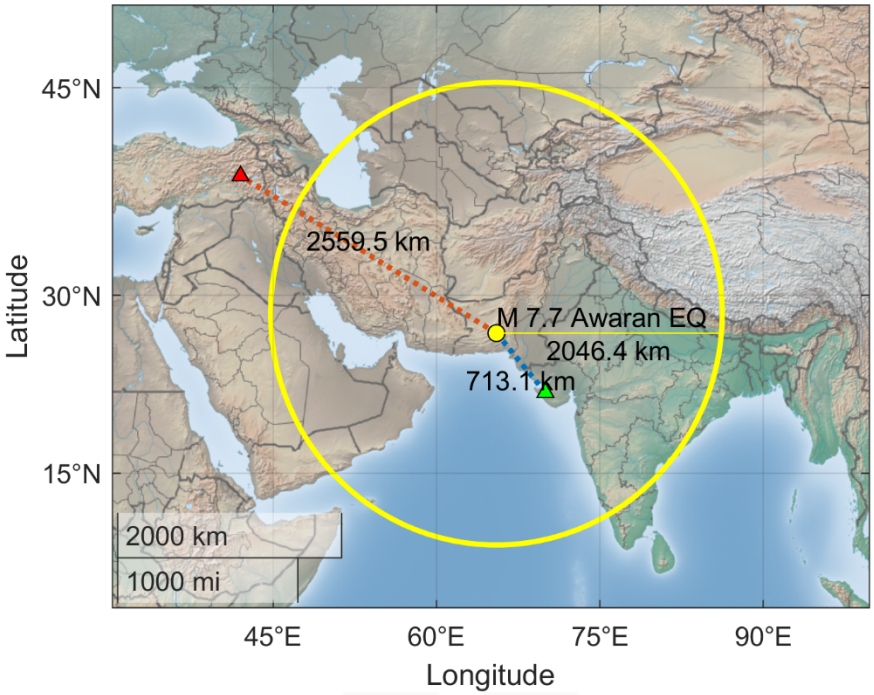

Figure 1. The location of selected points. The small yellow circle indicates the epicenter, the green triangular shows the point located within EPA, and the red triangular shows the point located outside EPA. The big yellow circle demonstrates the EPA of the Awaran earthquake.

The TEC values at the selected points are calculated by the 4-point bivariate interpolation method (Schaer et al., 1998). In this method, we used the nearest four grid points to the point of interest in the Global Ionosphere Maps (GIMs) provided by the International GNSS Service (IGS).

$$TEC(\lambda_e,\beta_e)=\begin{bmatrix}1-|\lambda_e-\lambda_0|/\Delta\lambda_{GIM} & |\lambda_e-\lambda_0|/\Delta\lambda_{GIM}\end{bmatrix}\begin{bmatrix}TEC_{00} & TEC_{01}\\ TEC_{10} & TEC_{11}\end{bmatrix}\begin{bmatrix}1-|\beta_e-\beta_0|/\Delta\beta_{GIM}\\ |\beta_e-\beta_0|/\Delta\beta_{GIM}\end{bmatrix} \quad (1)$$

where β_e,λ_e are geocentric coordinates of the point of interest, β_0,λ_0 are the geocentric coordinates of the nearest grid points, $\Delta\beta_{GIM},\Delta\lambda_{GIM}$ are spatial resolutions of the GIMs (generally 2.5 and 5 degrees, respectively), $TEC_{00},TEC_{01},TEC_{10},TEC_{11}$ are TEC values of the nearest grid points.

The TEC time series was divided into three segments for our analysis: 1) The data from August 1 to September 14, 2013, was utilized to train the model. 2) The data from September 14 to September 19, 2013, was selected to evaluate the model's accuracy. 3) The data from September 19 to September 26, 2013, represented the actual data used for TEC forecasting, anomaly detection, and assessing differences.

Significant changes in ionospheric variations are induced by disrupted space weather conditions. Therefore, it is crucial to monitor space weather changes while investigating the seismic-induced effects on the ionosphere. In our study, we incorporated several indices, including Kp, disturbance storm time (Dst), solar radio flux (F10.7), and solar wind speed (V_{SW}), to examine the impact of space weather conditions on ionospheric anomalies during the pre-earthquake period.

1.1.1. Solar and geomagnetic conditions before the Awaran earthquake

The time series of the Dst, V_{SW}, Kp, and F10.7 indices are investigated between September 19-24, 2013, due to the possibility that disturbed space weather before the earthquake may mask seismic-related changes in the TEC time series. Figure 2a and 2c show the time series of Dst and Kp geomagnetic activity indices. While Dst values range between ±20 nT and Kp values are less than 4 (except for September 19 and 24) which indicates the quiet geomagnetic activity before the earthquake. Figure 2b and 2d demonstrate the time series of V_{SW} and F10.7 solar activity indices. The V_{SW} values indicate a solar wind on September 19 and 20, the index values vary between 500-600 km/s. A solar wind becomes critical when exceeds 800 km/s which may be resulting geomagnetic disturbances on earth. According to Dst and Kp values, the level of V_{SW} values did not cause a significant geomagnetic instability. In addition, F10.7 values are between 105-115 sfu, indicating low solar activity before the earthquake.

1.2. Input Vector

The input vector in our model is represented as X_t, which corresponds to the TEC values. We adopt a time window of 12 observations, where each observation consists of TEC values collected at two-hour intervals over a single day. Thus, the values X_t=[TEC_1 TEC_2 ... TEC_t] are accessed by the input gate and utilized to predict the next observation, TEC_{t+1}, which serves as the output of the model.

In this context, the time span from 1 to t is referred to as time window t. During the first iteration or within this window, X_t is used as the input, while TEC_{t+1}, is the corresponding output. Subsequently, in the second iteration, X_{t+1}=[TEC_2 TEC_3 ... TEC_{t+1}] is utilized as the input, and the output at time window t+1 is TEC_{t+2}. This process continues iteratively for subsequent time windows.

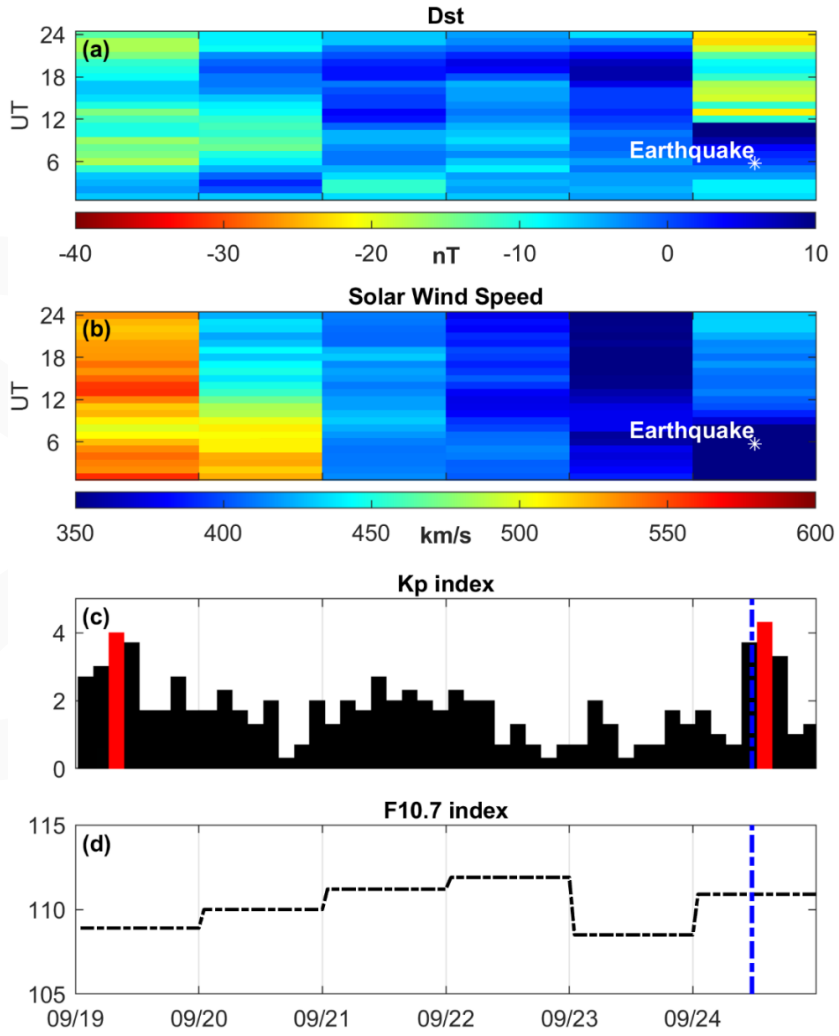

Figure 2. Space weather indices from September 19 to September 24, 2013. (a) Dst index (b) V_{SW} index (c) Kp index (d) F10.7 index. White asterisk in (a) and (b) and vertical blue dash-dotted lines in (c) and (d) demonstrate earthquake time.

1.2.1. Weight vector for input

The weight vector for input, denoted as W_t, holds utmost significance in our model. It comprises four distinct weight vectors, one for each gate, and can be expressed as $W_t=[w_f\ w_i\ w_c\ w_o]^T$. Here, w_f represents the weights for the forget gate, w_i corresponds to the input gate, w_c pertains to the cell state, and w_o denotes the output gate. The dimensionality of w_f, along with the other three weight vectors, aligns with the number of elements in the input vector, X_t. Throughout the process, this weight vector is multiplied with the input vector and subsequently applied to sigmoid or hyperbolic tangent (tanh) functions.

1.2.2. Output weight vector

Similar to the input weight vector, the output weight vector is another crucial parameter denoted as $O_t=[O_f\ O_i\ O_c\ O_o]^T$, where the symbols represent the output vector for different gates. The distinction between the weight vector and the output vector lies in the fact that the output vector is multiplied by the output at time t-1 during the training process. Additionally, the dimensionality of the output weight vector is 1, as we are predicting only one term as the output, which is TEC_{t+1}.

1.2.3. Bias vector

Bias is a set of vector terms that are employed to offset and minimize the bias inherent in the gate functions. It is represented as $b_t=[b_f\ b_i\ b_c\ b_o]^T$, where b_f and the remaining three elements represent the biases for each respective gate. Unlike the weight vectors, the biases have a singular value for each gate, rather than being represented as vectors.

1.2.4. Hyperparameter tuning

Finding optimal hyperparameters for deep learning algorithms can be challenging due to the lack of a systematic and effective approach. However, two commonly used strategies are Randomized CV Search (RCS) and Grid CV Search (GCS). GCS involves trying out all possible combinations of hyperparameter values to select the best one. However, with a large number of hyperparameters, like in deep learning algorithms, it becomes impractical to test every combination.

To address this, we employed the RCS method, where the model developer randomly assigns values to the hyperparameters and evaluates the model's performance. However, determining the ideal values for each hyperparameter remains a challenge. The main hyperparameters in our proposed model include Epoch, Batch size, Dropout, Learning rate, hidden layers, and nodes. We used RCS to determine their values. For example, we set the Epoch by monitoring the Mean Squared Error (MSE) until it drops below 0.02 (as shown in Figure 5). The Batch size of 12 was chosen to capture daily patterns in the TEC data. A Dropout value of 0.2 was selected to reduce overfitting by dropping 20% of nodes in the hidden layers. A learning rate of 0.1 (denoted as λ) was chosen to ensure a balance between convergence speed and avoiding overshooting the minima. Determining the optimal number of hidden layers and nodes involved multiple iterations of the model and evaluating various metrics, which will be discussed in the evaluation criteria section below.

1.2.5. Cost/loss function

We have used the MSE score to judge the model during training. The formula for MSE is defined in the Evaluation Criteria section.

1.3. Model Formulation

The proposed model, LSTM, is an extension of RNN which overcomes the problem of vanishing gradient. The special architectures of the LSTM-RNN network keep learning the data points that are far from the forecasting point within the network and prediction based on this learning. LSTM has various components which can forget or store information.

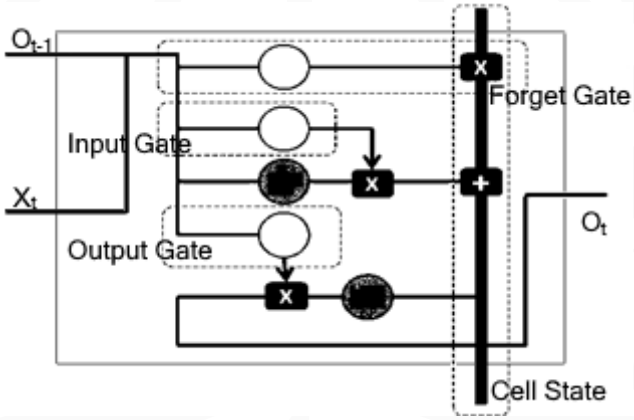

Figure 3. Node architecture for LSTM network.

Let the input is X_t, weight vector $W_t=[w_f, w_i, w_c, w_o]$, bias $b_t=[b_f, b_i, b_c, b_o]$, and output O_t at time t. In the first step of the LSTM, the unnecessary information for the cell state is decided by a sigmoid layer called the forget gate layer.

$$f_t = \sigma(w_f[O_{t-1}, X_t] + b_f) \tag{2}$$

In the next step, the values that need to be updated are selected by a sigmoid layer called the input gate layer, and then a tanh layer creates a vector of new candidate values to store new information in the cell state.

$$i_t = \sigma(w_i[O_{t-1}, X_t] + b_i) \tag{3}$$

$$\tilde{C_t} = \tanh(w_c[O_{t-1}, X_t] + b_c) \tag{4}$$

Now, to update the old cell state into the new cell state, the old cell state (C_{t-1}) is multiplied by f_t, and $i_t \tilde{C_t}$ showing the candidate values scaled with each updated state value is added.

$$C_t = f_t C_{t-1} + i_t \tilde{C_t} \tag{5}$$

Finally, we put the new cell state in tanh (values are normalized between -1 and 1) and, multiplying by the sigmoid gate, so we decide the information to be transferred from the cell state to the output gate.

$$h_t = \sigma(w_0[O_{t-1}, X_t] + b_0) \tag{6}$$

$$O_t = h_t \tanh(C_t) \tag{7}$$

While standard RNN networks have only a single tanh layer, LSTM networks contain four different layers that are: Cell State, Input Gate, Forget Gate, and Output Gate. To implement the proposed model, code written in Python.3 using Keras library, debugged on Jupyter Notebook which can be download from the link: https://jupyter.org/.

1.3.1. Detailed architecture of LSTM

In Figure 4, we are representing the detailed architecture of the proposed model. The input vector (t_1) is passed to the input layer and then the feed-forward process begins. After successfully predicted the TEC values, we calculate error and start tuning the parameters of the model which is a backpropagation process.

1.3.2. Evaluation criteria

Various metrics were employed to evaluate the performance of the purposed model; Mean Square Error (MSE), Root Mean Square Error (RMSE), Normalized Mean Square Error (NMSE), Normalized Root Mean Square Error (NRMSE), and Standard Deviation (SD). The calculation methods for each are the following:

$$MSE = \frac{1}{n}\sum_{i=1}^{n}(TEC_{Predicted} - TEC_{Actual})^2 \tag{8}$$

$$RMSE = \sqrt{\frac{1}{n}\sum_{i=1}^{n}(TEC_{Predicted} - TEC_{Actual})^2} \tag{9}$$

$$NMSE = \frac{MSE}{[\max(TEC_{Actual}) - \min(TEC_{Actual})]} \tag{10}$$

$$NRMSE = \frac{RMSE}{[\max(TEC_{Actual}) - \min(TEC_{Actual})]} \tag{11}$$

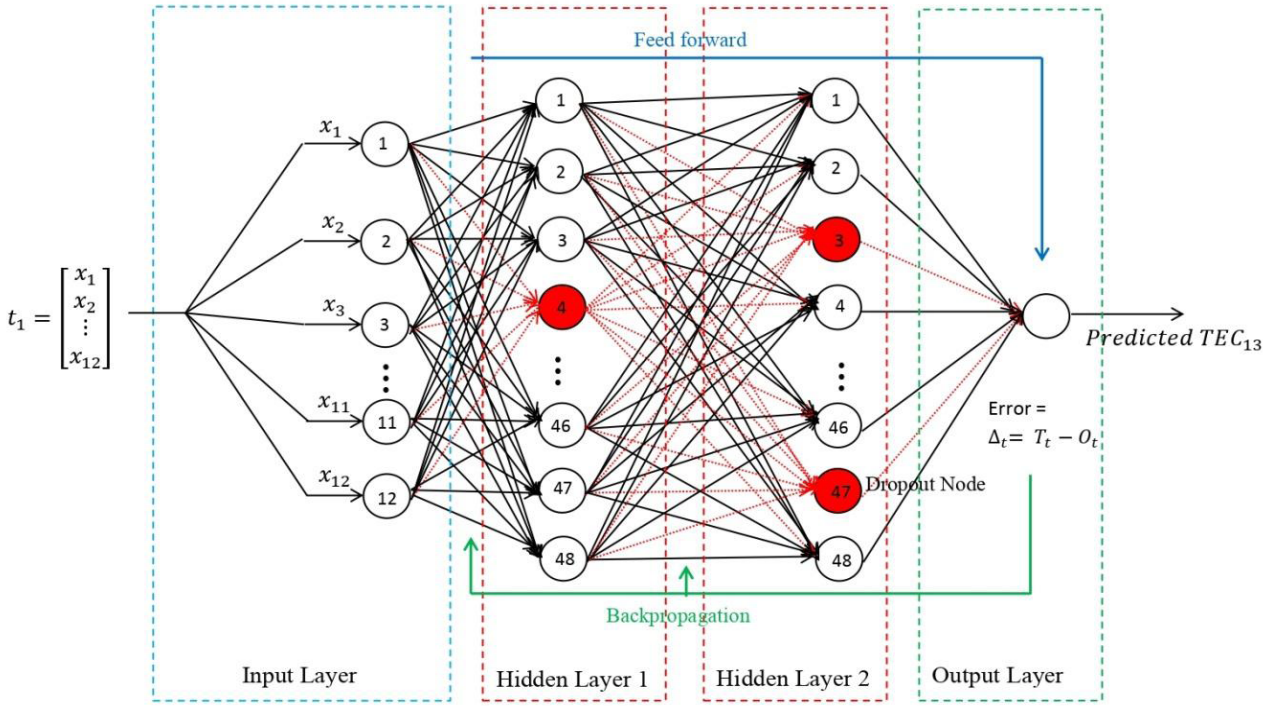

Figure 4. Detailed architecture of LSTM. Red color nodes and dashed edges represent the nodes that are dropout during the process of training the model.

NRMSE used a normalized scale to facilitate the comparison among different models. RMSE and NRMSE both have some kind of error estimation but NRMSE is the division of difference between the maximum and minimum value of the whole series. Suppose, if the last values of the series are scaled so much compare to the first few values then the RMSE score will be high. Hence, NRMSE is normalized using the difference and used to compare with other models. Unfortunately, no other studies presented their NRMSE score of the model so we are failed to compare but future studies may use NRMSE to compare with the proposed model.

$$SD = \sqrt{\frac{1}{n-1}\sum_{i=1}^{n}\left(TEC_{Actual} - \underline{TEC_{Actual}}\right)^2} \tag{12}$$

where n is the number of observations involves in evaluating the model and $\underline{TEC_{Actual}}$ is the value of mean for actual TEC observations employed for evaluation.

2. RESULTS AND DISCUSSIONS

In our approach, we implemented LSTM model with two hidden layers, each consisting of 48 nodes. We incorporated a dropout rate of 20% to mitigate overfitting. For training, we utilized a batch size of 12 observations, representing the number of data points in a single day. Additionally, we allocated 30% of the data for validation purposes.

To optimize the LSTM model's performance, we employed the Adam Optimizer to update the hyper-parameters. The MSE metric was utilized to assess and improve the accuracy of our model.

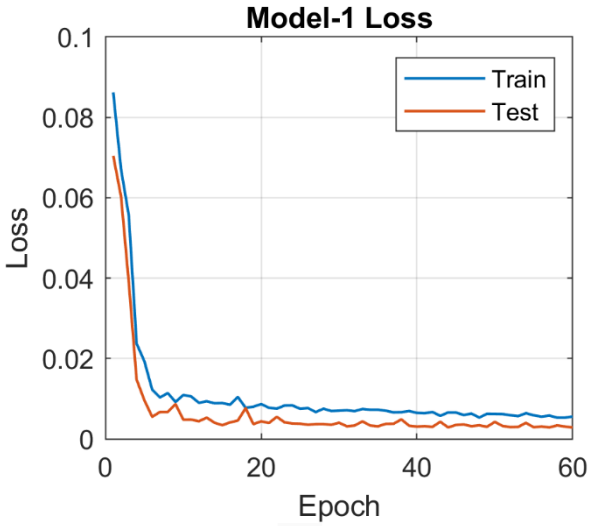

Figure 5. Training of model.

In Figure 5, we are representing the training phase of the model. As shown, there are two curves: blue depicts the loss of training data and red color shows the loss of evaluation data prediction. With the increasing number of Epoch, loss in prediction is decreasing and reached at a level around zero. Therefore, we can say that our model is trained enough to estimate the TEC values after sixty Epoch.

We implemented our model and conducted an evaluation using a separate set of data. Table 2 presents the different metrics we used to assess the model's performance. The RMSE was found to be 3.51, indicating good accuracy. The NRMSE was calculated to be 0.07.

To forecast TEC values leading up to the earthquake, we plotted the results in the upper panel of Figure 6. By comparing the observed TEC values with the forecasted ones, we calculated the differences. Any errors that exceeded a predefined threshold were considered anomalies. The threshold was determined through statistical analysis, considering the mean and standard deviation.

It is important to note that diurnal variations in ionospheric TEC depend on various factors, making it challenging to assume a normal distribution of the data. However, by applying statistical methods, such as considering values outside the range of $\mu \pm 2\sigma$ (with a 95% confidence level), we can identify

anomalies (Li et al., 2009; Adil et al., 2021). In the bottom panel of Figure 6, a strong positive anomaly is highlighted in red on September 21, 2013, three days prior to the earthquake.

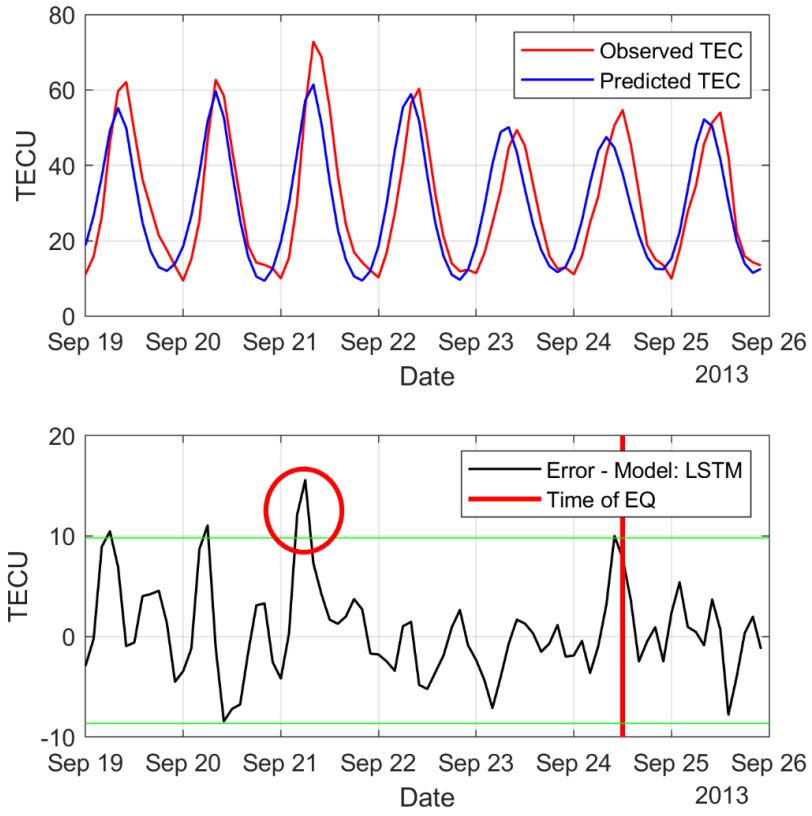

Figure 6. Observed and predicted TEC values (top) and errors calculated on the epicenter location (bottom) from September 19 to September 26, 2013. The red circles indicate anomalies according to $\mu \pm 2\sigma$, where μ is the mean of errors and σ is the standard deviation of errors.

Table 2. Matrices of the proposed model.

Matrices	MSE	RMSE	NMSE	NRMSE	SD
Epicenter	12.34	3.51	0.25	0.07	3.24
Within EPA	20.81	4.56	0.31	0.06	4.43
Outside EPA	5.59	2.36	0.25	0.10	2.25

All these analyses take place at the epicenter of the earthquake. In the case of generating an alarm about the ionospheric perturbation-based earthquake, we will not aware of the epicenter. So in this case, we change the case a little bit and start analyzing nearby areas of the epicenter as well as outside the EPA. We have conducted the following two experiments:

2.1. Within EPA

In order to analyze within EPA, we have picked out some locations nearby the epicenter and found similar results with minor changes. We captured the TEC values and train the model. Once, training is completed, we forecast for the evaluation set and evaluate the model on the metrics defined in Table 1. In this experiment, anomalies are detected on the same day (September 21, 2013) with comparatively less intensity that is consistent with the epicentral analysis. Moreover, we have also found positive and negative anomalies one day before the leading anomaly happened on September 20, 2013. In Figure 7, the anomalies are demonstrated in red color circles. It shows that if we monitor in some block radius, we will surely observe the abnormality in the TEC data.

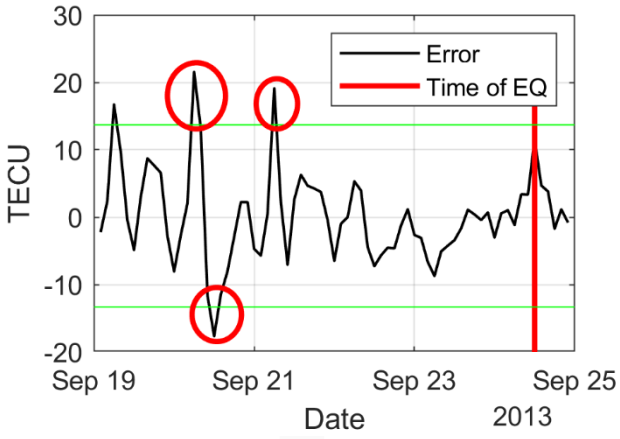

Figure 7. Errors calculated within EPA. The red circles indicate anomalies according to $\mu \pm 2\sigma$, where μ is the mean of errors and σ is the standard deviation of errors.

2.2. Outside EPA

We also need to analyze the earthquake effects outside the EPA, although in the above experiments anomalies are successfully detected. We trained and forecast the TEC values with 2.36 and 0.25 RMSE and NRMSE scores, respectively (Table 1). Then forecast the TEC with the same time window. We found that there is no perturbation before the earthquake and everything seems normal (Figure 8). There is a strong anomaly after the earthquake which is not associated with the Awaran earthquake where the Kp index is 4 on September 24, 2013, it is thought to be caused by a minor geomagnetic storm that affects this location (see Figure 2).

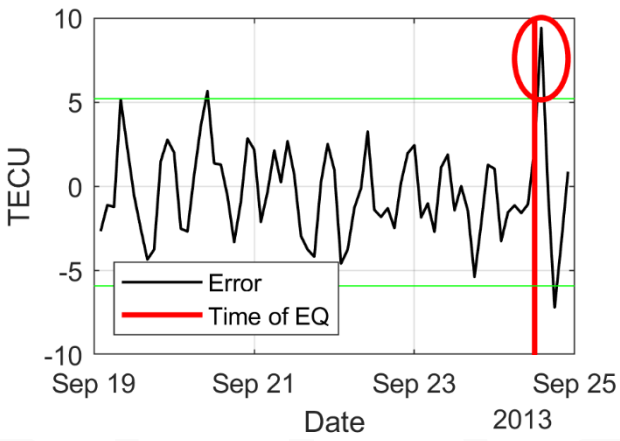

Figure 8. Errors calculated outside EPA. The red circles indicate anomalies according to μ±2σ, where μ is the mean of errors and σ is the standard deviation of errors.

The analysis of Figures 6, 7, and 8 reveals valuable insights into the relationship between TEC anomalies and seismic activity in the context of the Awaran earthquake in 2013. Figure 6 demonstrates a noteworthy positive TEC anomaly three days prior to the earthquake, suggesting a potential link between ionospheric disturbances and impending seismic events. Figure 7 extends this analysis to the EPA, showing consistent anomalies on the same day and one-day prior, emphasizing the importance of monitoring specific geographic regions for early warning systems. In contrast, Figure 8 reveals that TEC anomalies were not detectable in areas outside the EPA before the earthquake, highlighting the significance of spatial context. Additionally, the post-earthquake anomaly in Figure 8 underscores the need to consider other geophysical factors, like geomagnetic storms, in interpreting ionospheric anomalies. Collectively, these figures underscore the potential of TEC data for seismic precursor detection but also emphasize the critical role of location and the need to account for external influences in such analyses.

2.3. Model Comparison

Various models have been already covered the issues using various algorithms, but the proposed model is more advance, accurate and reliable. Autoregressive Integrated Moving Average (ARIMA) is strongest among all known machine learning approaches for time-series analysis like Autoregressive (AR), Moving Average (MA), Autoregressive Moving Average (ARMA). However, after being introduced to deep learning, ANN has enhanced the accuracy significantly. Many studies have been proposed on ANN on TEC forecasting but ANN was not enough to capture long-term dependency of data. For instance, our TEC data is nothing but a time series therefore value at time-0 (T0) can affect value far away from T0. RNN came into the picture to overcome the problem however it was also suffering from the problem of vanishing and exploding gradient. Afterward, LSTM overcame the issue and we are using LSTM with optimizing hyperparameter tuning that is why the proposed model can

be considered more advanced than previous studies. In Table 3, we have implemented few algorithms of them and compare their metrics. AR is the worst performer and ARIMA gives comparatively less error (Saqib et al., 2021). However, the proposed model has 3.25 and 0.06 RMSE and NRMSE score, respectively which is an indication of that proposed model significantly better than other.

Table 2. Performance comparison of various AI methods with the proposed method.

Metrics / Methods	AR	MA	ARIMA	LSTM
MSE	145.1911	215.5111	89.6136	10.6162
RMSE	12.0495	14.6802	9.4664	3.2582
NMSE	2.9289	4.3474	1.8077	0.2216
NRMSE	0.243	0.2961	0.1909	0.068

CONCLUSION

In the present study, we have implemented an AI-based technique, LSTM, to forecast ionospheric TEC values. The data of TEC values employed for the study is recorded by GNSS observations. The proposed model forecast TEC values for normal days and we can get the anomalies by comparing with actual values. We forecast the TEC values using LSTM with 3.51 and 0.25 RMSE and NRMSE scores, respectively.

In our case, we detected pre-seismic anomalies 3 days before the Awaran earthquake at the epicenter and a point within EPA. Also, there is no clear anomaly at the point of outside EPA. In practical applications, we don't know where the earthquake will happen. So, we tested three points and showed pre-earthquake anomalies in EPA. According to Adil et al. (2021c), the lithosphere-ionosphere coupling (LAIC) is a mutual interaction of different geophysical shells within the earth's atmosphere, specifically, over the earthquake epicenter and its preparation area inducing a layer-to-layer conjugation. In this sense, the presence of the ionospheric earthquake-induced anomalies should appear within the earthquake preparation area, while the rest of the surrounding ionosphere should pose regular variability. Therefore, we choose two points one within the preparation region and the other is outside the seismogenic region. In order to understand the LAIC, Pulinets and Ouzounov (2011) proposed a radon exhalation-based theory by explaining the mutual interaction of radon decayed electron particles and atmospheric constituents. As a result of these processes the vertical electric field changes the electrical conductively of the atmosphere which contributes to the electrical dynamics of the ionosphere. This theory was later confirmed by Adil et al. (2021c) by using layer-to-layer robust satellite data. Our results have suggested a clear demonstrated of the Adil et al. (2021c)'s model and findings, as the TEC anomalies are present within the preparation area while towards the outside of

the preparation area, we experience a regular trend in the TEC values without a subtle change. The proposed strategy additionally helps to distinguish ionospheric anomalies caused by space weather from those caused by earthquakes, because space weather caused the global ionospheric variations compared to the localized phenomena of seismo-ionospheric coupling. Thus, we have theoretically revealed that seismo-ionospheric anomalies are seen within EPA and they are not seen outside EPA. It reveals the separating power of the LSTM approach for local ionospheric anomalies. The proposed method may also be preferred for studies of regional ionosphere and space weather.

The results from the present study showed that LSTM networks successfully revealed both earthquake and space weather-induced ionospheric variations. Such a proposed model can be proposed as a new methodology for setting up an earthquake warning system. In addition, predicted TECs will be a cutting-edge science for future ionospheric studies in natural hazards (e.g. earthquake, tsunami, typhoon, volcano), space weather, navigation, and telecommunications.

Acknowledgment

This research is supported by the National Natural Science Foundation of China Research Fund for International Young Scientists Grant no. 42250410331.

Data Availability

All the datasets used in the study are publicly available at the following online links:

ftp://cddis.nasa.gov/gnss/products/ionex/ (GIM products for TEC estimation)

https://omniweb.gsfc.nasa.gov/form/dx1.html (Space weather indices)

https://www.ngdc.noaa.gov/hazard/ (Details of the earthquake)

REFERENCES

Adeli, H., & Panakkat, A. (2009, September). A probabilistic neural network for earthquake magnitude prediction. Neural Networks, 22(7), 1018–1024. https://doi.org/10.1016/j.neunet.2009.05.003

Adil, M. A., Abbas, A., Ehsan, M., Shah, M., Naqvi, N. A., & Alie, A. (2021, May). Investigation of ionospheric and atmospheric anomalies associated with three M >6.5 EQs in New Zealand. Journal of Geodynamics, 145, 101841. https://doi.org/10.1016/j.jog.2021.101841

Adil, M. A., Şentürk, E., Shah, M., Naqvi, N. A., Saqib, M., & Abbasi, A. R. (2021, October). Atmospheric and ionospheric disturbances associated with the M > 6 earthquakes in the East Asian sector: A case study of two consecutive earthquakes in Taiwan. Journal of Asian Earth Sciences, 220, 104918. https://doi.org/10.1016/j.jseaes.2021.104918

Adil, M. A., Şentürk, E., Pulinets, S. A., & Amory-Mazaudier, C. (2021, September). A Lithosphere–Atmosphere–Ionosphere Coupling Phenomenon Observed Before M 7.7 Jamaica Earthquake. Pure and Applied Geophysics, 178(10), 3869–3886. https://doi.org/10.1007/s00024-021-02867-z

Akhoondzadeh, M., Parrot, M., & Saradjian, M. R. (2010, January). Electron and ion density variations before strong earthquakes (M>6.0) using DEMETER and GPS data. Natural Hazards and Earth System Sciences, 10(1), 7–18. https://doi.org/10.5194/nhess-10-7-2010

Akhoondzadeh, M. (2013, August). Genetic algorithm for TEC seismo-ionospheric anomalies detection around the time of the Solomon (Mw=8.0) earthquake of 06 February 2013. Advances in Space Research, 52(4), 581–590. https://doi.org/10.1016/j.asr.2013.04.012

Asaly, S., Gottlieb, L. A., Inbar, N., & Reuveni, Y. (2022, June). Using Support Vector Machine (SVM) with GPS Ionospheric TEC Estimations to Potentially Predict Earthquake Events. Remote Sensing, 14(12), 2822. https://doi.org/10.3390/rs14122822

Athukorala, P. C., & Resosudarmo, B. P. (2005, January). The Indian Ocean Tsunami: Economic Impact, Disaster Management, and Lessons. Asian Economic Papers, 4(1), 1–39. https://doi.org/10.1162/asep.2005.4.1.1

Beyreuther, M., & Wassermann, J. (2008, December). Continuous earthquake detection and classification using discrete Hidden Markov Models. Geophysical Journal International, 175(3), 1055–1066. https://doi.org/10.1111/j.1365-246x.2008.03921.x

Draz, M. U., Shah, M., Jamjareegulgarn, P., Shahzad, R., Hasan, A. M., & Ghamry, N. A. (2023, April). Deep Machine Learning Based Possible Atmospheric and Ionospheric Precursors of the 2021 Mw 7.1 Japan Earthquake. Remote Sensing, 15(7), 1904. https://doi.org/10.3390/rs15071904

Dilmaghani, T.M. (2020). Modelling of relation between large earthquakes and ionosphere electron density using GPS data. Journal of Artificial Intelligence in Electrical Engineering, 9(33), 8-19.

Dobrovolsky, I. P., Zubkov, S. I., & Miachkin, V. I. (1979). Estimation of the size of earthquake preparation zones. Pure and Applied Geophysics PAGEOPH, 117(5), 1025–1044. https://doi.org/10.1007/bf00876083

Freeshah, M., Zhang, X., Şentürk, E., Adil, M. A., Mousa, B. G., Tariq, A., Ren, X., & Refaat, M. (2021, February). Analysis of Atmospheric and Ionospheric Variations Due to Impacts of Super Typhoon Mangkhut (1822) in the Northwest Pacific Ocean. Remote Sensing, 13(4), 661. https://doi.org/10.3390/rs13040661

Guo, J., Li, W., Yu, H., Liu, Z., Zhao, C., & Kong, Q. (2015, October). Impending ionospheric anomaly preceding the Iquique Mw8.2 earthquake in Chile on 2014 April 1. Geophysical Journal International, 203(3), 1461–1470. https://doi.org/10.1093/gji/ggv376

Hafeez, A., Ehsan, M., Abbas, A., Shah, M., & Shahzad, R. (2022, January). Machine learning-based thermal anomalies detection from MODIS LST associated with the Mw 7.7 Awaran, Pakistan earthquake. Natural Hazards, 111(2), 2097–2115. https://doi.org/10.1007/s11069-021-05131-8

Hattori, K., Hirooka, S., Kunimitsu, M., Ichikawa, T., & Han, P. (2014, August). Ionospheric anomaly as an earthquake precursor: Case and statistical studies during 1998–2012 around Japan. In 2014 XXX-Ith URSI General Assembly and Scientific Symposium (URSI GASS) (pp. 1-1). IEEE.

Hsiao, C. C., Liu, J. Y., Oyama, K. I., Yen, N. L., Liou, Y. A., Chen, S. S., & Miau, J. J. (2009, June). Seismo-ionospheric precursor of the 2008 Mw7.9 Wenchuan earthquake observed by FORMOSAT-3/COSMIC. GPS Solutions, 14(1), 83–89. https://doi.org/10.1007/s10291-009-0129-0

Li, J., Meng, G., Wang, M., Liao, H., & Shen, X. (2009, October). Investigation of ionospheric TEC changes related to the 2008 Wenchuan earthquake based on statistic analysis and signal detection. Earthquake Science, 22(5), 545–553. https://doi.org/10.1007/s11589-009-0545-9

Li, X., Zheng, K., Li, X., Liu, G., Ge, M., Wickert, J., & Schuh, H. (2018, December). Real-time capturing of seismic waveforms using high-rate BDS, GPS and GLONASS observations: the 2017 Mw 6.5 Jiuzhaigou earthquake in China. GPS Solutions, 23(1). https://doi.org/10.1007/s10291-018-0808-9

Li, W., Yue, J., Wu, S., Yang, Y., Li, Z., Bi, J., & Zhang, K. (2018, April). Ionospheric responses to typhoons in Australia during 2005–2014 using GNSS and FORMOSAT-3/COSMIC measurements. GPS Solutions, 22(3). https://doi.org/10.1007/s10291-018-0722-1

Li, W., Narvekar, N., Nakshatra, N., Raut, N., Sirkeci, B., & Gao, J. (2018, March). Seismic data classification using machine learning. In 2018 IEEE Fourth International Conference on Big Data Computing Service and Applications (BigDataService) (pp. 56-63). IEEE.

Li, Z., Meier, M., Hauksson, E., Zhan, Z., & Andrews, J. (2018, May). Machine Learning Seismic Wave Discrimination: Application to Earthquake Early Warning. Geophysical Research Letters, 45(10), 4773–4779. https://doi.org/10.1029/2018gl077870

Liu, J. Y., Yang, W. H., Lin, C. H., Chen, Y. I., & Lee, I. T. (2013, June). A statistical study on the characteristics of ionospheric storms in the equatorial ionization anomaly region: GPS-TEC observed over Taiwan. Journal of Geophysical Research: Space Physics, 118(6), 3856–3865. https://doi.org/10.1002/jgra.50366

Liu, J. Y., Chen, C. Y., Sun, Y. Y., Lee, I. T., & Chum, J. (2019, May). Fluctuations on vertical profiles of the ionospheric electron density perturbed by the March 11, 2011 M9.0 Tohoku earthquake and tsunami. GPS Solutions, 23(3). https://doi.org/10.1007/s10291-019-0866-7

Melgarejo-Morales, A., Esteban Vazquez-Becerra, G., Millan-Almaraz, J., Martinez-Felix, C. A., & Shah, M. (2023, November). Applying support vector machine (SVM) using GPS-TEC and Space Weather parameters to distinguish ionospheric disturbances possibly related to earthquakes. Advances in Space Research, 72(10), 4420–4434. https://doi.org/10.1016/j.asr.2023.08.028

Ouzounov, D., Pulinets, S., Romanov, A., Romanov, A., Tsybulya, K., Davidenko, D., Kafatos, M., & Taylor, P. (2011, December). Atmosphere-ionosphere response to the M9 Tohoku earthquake revealed by multi-instrument space-borne and ground observations: Preliminary results. Earthquake Science, 24(6), 557–564. https://doi.org/10.1007/s11589-011-0817-z

Pulinets, S., & Ouzounov, D. (2011, June). Lithosphere–Atmosphere–Ionosphere Coupling (LAIC) model – An unified concept for earthquake precursors validation. Journal of Asian Earth Sciences, 41(4–5), 371–382. https://doi.org/10.1016/j.jseaes.2010.03.005

Saqib, M., Şentürk, E., Sahu, S. A., & Adil, M. A. (2022, January). Comparisons of autoregressive integrated moving average (ARIMA) and long short term memory (LSTM) network models for ionospheric anomalies detection: a study on Haiti (Mw = 7.0) earthquake. Acta Geodaetica Et Geophysica, 57(1), 195–213. https://doi.org/10.1007/s40328-021-00371-3

Saqib, M., Şentürk, E., Sahu, S. A., & Adil, M. A. (2021, June). Ionospheric anomalies detection using autoregressive integrated moving average (ARIMA) model as an earthquake precursor. Acta Geophysica, 69(4), 1493–1507. https://doi.org/10.1007/s11600-021-00616-3

Schaer, S., Gurtner, W., Feltens, J. (1998, February). IONEX: The ionosphere map exchange format version 1. In Proceedings of the IGS AC workshop, Darmstadt, Germany (Vol. 9, No. 11).

Shi, K., Ding, H., Guo, J., & Yu, T. (2021, April). Refined seismic-ionospheric effects: case study of Mw 8.2 Chiapas earthquake on September 7, 2017. GPS Solutions, 25(3). https://doi.org/10.1007/s10291-021-01129-8

Zhukov, A. V., Yasyukevich, Y. V., & Bykov, A. E. (2021). GIMLi: Global Ionospheric total electron content model based on machine learning. GPS Solutions, 25(1). https://doi.org/10.1007/s10291-020-01055-1